ICCFD13-2026-297

A Time-Accurate Local Time-Stepping DG Scheme with a Multistep, Multistage Continuous-Explicit Temporal Predictor

S. Liu*, K. Zhang** and X. Qin†
Corresponding author: liushihao@iet.cn; zkl70@buaa.edu.cn; qinxueyu@iet.cn
* Department of Mathematics, Linné FLOW Centre, KTH Royal Institute of Technology, 100 44, Stockholm, Sweden.
** School of Aeronautic Science and Engineering, Beihang University, Beijing, 100191, PR China.
† Digital Twin Research Center, Institute of Engineering Thermophysics, Chinese Academy of Sciences, Beijing 100190, PR China.

Abstract: This paper constructs a multistep, multistage continuous-explicit Runge–Kutta (MSCERK) temporal predictor and applies it within a time-accurate local time-stepping discontinuous Galerkin (LTS-DG) framework. The motivation comes from temporally multiscale unsteady flows, where a global explicit time step is often dictated by the most restrictive local time scale and therefore leads to redundant updates in the rest of the domain. In the LTS-DG predictor–corrector framework, each element requires a continuous-in-time local predictor so that interface fluxes can be integrated consistently from neighboring states at asynchronous time levels. The constructed MSCERK predictor uses both current-step and previous-step information to build this continuous representation. In particular, the two-step MSCERK construction reduces the number of current-step predictor stages required for a prescribed continuous order, making it well suited for LTS-DG calculations in which stage residual evaluations dominate the cost. The order conditions of the two-step continuous extension are summarized, and representative numerical tests are reported to demonstrate accuracy and efficiency.

Keywords: Local time stepping, discontinuous Galerkin method, continuous explicit Runge–Kutta method, multistep temporal predictor, high-order methods.

1. Introduction

Temporal discretization schemes include multistage, multistep, and multiderivative methods, represented by classical Runge–Kutta (RK) schemes, linear multistep methods (LMMs), and Lax–Wendroff/Cauchy–Kowalevski (CK) approaches, respectively. Recent research has further explored hybrid combinations of these categories, such as two-step Runge–Kutta (TSRK) methods and related extensions for hyperbolic conservation laws [1, 2, 3].

High-order discontinuous Galerkin (DG) methods combine element-local polynomial approximation with numerical fluxes at element interfaces, yielding a locally conservative, high-order accurate framework that is well suited for complex geometries, unstructured meshes, and parallel computing [4, 5, 6, 7, 8]. For time-dependent problems, DG methods are typically coupled with explicit time integration. Their overall efficiency is therefore strongly influenced by the allowable time step, which depends on the smallest local mesh size, the local wave speed, and the polynomial order.

In practical engineering flow simulations, the relevant time scales are often strongly multiscale and spatially nonuniform. A global explicit time step may then be dictated by a small subset of restrictive cells, for example near shocks, boundary layers, locally refined regions, or narrow geometric gaps. As a consequence, large portions of the domain are advanced with unnecessarily small time steps, which

introduces substantial computational redundancy in long-time unsteady simulations.

Local time stepping (LTS) alleviates this bottleneck by allowing different elements to advance with different local time steps through subcycling or hierarchical time grids. Its key difficulty is the loss of time synchronization across interfaces. Numerical fluxes [9], especially fluxes that must be integrated in time, have to be matched consistently over different time intervals in order to maintain conservation and time accuracy.

Most LTS-DG methods can be formulated in a predictor–corrector manner. A local predictor provides a time-continuous representation within each element, and a corrector couples neighboring elements by integrating interface fluxes over the appropriate face-wise time intervals [10, 11, 12]. For this predictor, Cauchy–Kowalevski-type constructions and continuous explicit Runge–Kutta (CERK) constructions are common choices [13, 10, 11, 14]. At high continuous order, however, the number of predictor-stage right-hand-side evaluations can become a major cost in LTS-DG calculations.

The purpose of this work is to reduce this predictor cost while retaining the time-continuous structure needed by LTS-DG. We develop a multistep, multistage continuous-explicit Runge–Kutta predictor, referred to as MSCERK. By incorporating information from previous steps into the continuous-extension structure of the current step, MSCERK distributes the information required for a time-continuous representation across multiple time levels. This reduces the minimum number of stages required in the current step for a prescribed continuous order. The resulting predictor is then embedded into a time-accurate LTS-DG predictor–corrector formulation.

The remainder of this paper is organized as follows. Section 2 introduces the general MSCERK predictor form, the two-step order conditions, and representative MSCERK examples. Section 3 reviews the time-accurate LTS-DG framework and incorporates MSCERK as the local continuous predictor. Section 4 reports representative numerical results, and Section 5 concludes the paper.

2. MSCERK Predictor

2.1 General multistep, multistage form

Consider the autonomous ordinary differential equation

$$u'(t) = F(u(t)).$$

Let $\Delta t_n = t_{n+1} - t_n$. We denote a q-step, m-stage predictor by MSCERK(q, m), where q is the number of stored time levels and m is the number of stages associated with the current step, including the known state u^n. Hence the predictor uses $q + m - 1$ states in total. The stored states are written as

$$Y_\rho = u^{n-q+1+\rho}, \qquad \rho = 0, \dots, q-1, \tag{1}$$

so that $Y_{q-1} = u^n$. If $m > 1$, the additional current-step stages are written as

$$Y_i = \sum_{\nu=0}^{q-1} d_{i,\nu} Y_\nu + \Delta t_n \sum_{j=0}^{i-1} a_{ij} F(Y_j), \qquad i = q, \dots, q+m-2, \tag{2}$$

and

$$u(t_n + \Delta t_n \theta) = \sum_{\nu=0}^{q-1} e_\nu(\theta) Y_\nu + \Delta t_n \sum_{j=0}^{q+m-2} b_j(\theta) F(Y_j), \qquad 0 \le \theta \le 1. \tag{3}$$

Here the coefficients $d_{i,\nu}$ insert the stored solution values into each additional stage, a_{ij} are explicit stage-coupling coefficients, and $e_\nu(\theta)$ and $b_j(\theta)$ are the continuous-output weights. These coefficients may depend on the relevant step ratios when variable time steps are used.

2.2 Two-step multistage form and order conditions

For the two-step case, the stored solution values are

$$Y_0 = u^{n-1}, \qquad Y_1 = u^n.$$

Let

$$\alpha = \Delta t_n / \Delta t_{n-1}, \qquad \ell = \begin{pmatrix} -\alpha^{-1} \\ 0 \end{pmatrix}. \tag{4}$$

The two-step MSCERK$(2, m)$ form uses the additional stages

$$Y_i = d_{i,0} u^{n-1} + d_{i,1} u^n + \Delta t_n \sum_{j=0}^{i-1} a_{ij} F(Y_j), \qquad i = 2, \ldots, m, \tag{5}$$

$$u(t_n + \Delta t_n \theta) = e_0(\theta) u^{n-1} + e_1(\theta) u^n + \Delta t_n \sum_{j=0}^{m} b_j(\theta) F(Y_j). \tag{6}$$

For compactly stating the order conditions, the stored nodes are included as the first two rows by setting $(d_{0,0}, d_{0,1}) = (1, 0)$, $(d_{1,0}, d_{1,1}) = (0, 1)$, and the first two rows of A to zero. Denote $D = (d_{i,\nu}) \in \mathbb{R}^{(m+1)\times 2}$, $A = (a_{ij}) \in \mathbb{R}^{(m+1)\times(m+1)}$, $e(\theta) = (e_0(\theta), e_1(\theta))^T$, and $b(\theta) = (b_0(\theta), \ldots, b_m(\theta))^T$. The internal abscissae are

$$c = D\ell + A\mathbf{1}, \qquad C = \operatorname{diag}(c), \tag{7}$$

where vector powers are understood componentwise. Matching the Taylor expansion about t_n yields the conditions listed in Table 1, with all lower-order conditions also being required.

Table 1: Two-step MSCERK continuous-extension order conditions.

Order	Additional order conditions
1	$D\mathbf{1} = \mathbf{1}, \qquad e(\theta)^T \mathbf{1} = 1,$
	$e(\theta)^T \ell + b(\theta)^T \mathbf{1} = \theta.$
2	$c - D\ell - A\mathbf{1} = 0,$
	$\frac{1}{2} e(\theta)^T \ell^2 + b(\theta)^T c = \frac{\theta^2}{2}.$
3	$\frac{1}{3} e(\theta)^T \ell^3 + b(\theta)^T c^2 = \frac{\theta^3}{3},$
	$b(\theta)^T \left[\frac{1}{2} \left(c^2 - D\ell^2 \right) - Ac \right] = 0.$
4	$\frac{1}{4} e(\theta)^T \ell^4 + b(\theta)^T c^3 = \frac{\theta^4}{4},$
	$b(\theta)^T C \left[\frac{1}{2} \left(c^2 - D\ell^2 \right) - Ac \right] = 0,$
	$b(\theta)^T A \left[\frac{1}{2} \left(c^2 - D\ell^2 \right) - Ac \right] = 0,$
	$b(\theta)^T \left[\frac{1}{6} \left(c^3 - D\ell^3 \right) - \frac{1}{2} Ac^2 \right] = 0.$

2.3 Examples

The single-step multistage case, $q = 1$, is denoted by MSCERK$(1, m)$ and recovers the usual m-stage continuous explicit Runge–Kutta (CERK) predictor [14]:

$$Y_0 = u^n, \qquad Y_i = u^n + \Delta t_n \sum_{j=0}^{i-1} a_{ij} F(Y_j), \quad i = 1, \ldots, m-1, \qquad u(t_n + \Delta t_n \theta) = u^n + \Delta t_n \sum_{j=0}^{m-1} b_j(\theta) F(Y_j). \tag{8}$$

A two-step, one-stage second-order continuous predictor, denoted by MSCERK$(2, 1)$, is

$$Y_0 = u^{n-1}, \qquad Y_1 = u^n, \qquad u(t_n + \Delta t_n \theta) = u^n + \Delta t_n \left[-\frac{\alpha}{2} \theta^2 F(Y_0) + \left(\theta + \frac{\alpha}{2} \theta^2 \right) F(Y_1) \right]. \tag{9}$$

For $\theta = 1$ and a uniform step size, this reduces to the classical two-step Adams–Bashforth update.

A two-step, two-stage third-order MSCERK predictor, denoted by MSCERK$(2, 2)$, is

$$\begin{aligned} Y_0 &= u^{n-1}, \qquad Y_1 = u^n, \\ Y_2 &= u^n + a_1 \, \Delta t_n \, F(Y_0) + a_2 \, \Delta t_n \, F(Y_1), \\ u(t_n + \Delta t_n \theta) &= u^n + \Delta t_n \Big(b_0(\theta) \, F(Y_0) + b_1(\theta) \, F(Y_1) + b_2(\theta) \, F(Y_2) \Big), \end{aligned} \tag{10}$$

where

$$\begin{aligned} \alpha &= \Delta t_n / \Delta t_{n-1}, \qquad a_1 = -\alpha, \qquad a_2 = \sqrt{2} + \alpha, \\ b_0(\theta) &= -\frac{\alpha a_1}{a_1 - a_2} \, \theta^2 - \frac{\alpha^2 (a_1 + a_2)}{3(a_1 - a_2)} \, \theta^3, \\ b_1(\theta) &= \theta + \frac{3 + 6\alpha a_1}{6a_1 - 6a_2} \, \theta^2 + \frac{2\alpha(1 + a_1 \alpha + a_2 \alpha)}{6a_1 - 6a_2} \, \theta^3, \\ b_2(\theta) &= -\frac{1}{2a_1 - 2a_2} \, \theta^2 - \frac{\alpha}{3(a_1 - a_2)} \, \theta^3. \end{aligned} \tag{11}$$

A two-step, three-stage fourth-order predictor, denoted by MSCERK$(2, 3)$, is

$$\begin{aligned} Y_0 &= u^{n-1}, \qquad Y_1 = u^n, \\ Y_2 &= u^n + \Delta t_n \left(-\frac{9}{8\alpha} F(Y_0) - \frac{3}{8\alpha} F(Y_1) \right), \\ Y_3 &= u^n + \Delta t_n \left(-\frac{\alpha(4\alpha + 9)}{6} F(Y_0) + \left(1 + \frac{5\alpha}{6} + \frac{2\alpha^2}{9} \right) F(Y_1) + \frac{2\alpha(2\alpha + 3)}{9} F(Y_2) \right). \end{aligned} \tag{12}$$

The continuous output is

$$u(t_n + \Delta t_n \theta) = u^n + \Delta t_n \sum_{j=0}^{3} b_j(\theta) F(Y_j), \tag{13}$$

where

$$
\begin{aligned}
b_0(\theta) &= \frac{\alpha\theta^2\left(3\alpha\theta^2 - 4\alpha\theta + 6\theta - 9\right)}{6(\alpha+1)},\\
b_1(\theta) &= \frac{\theta\left(18 + (15\alpha - 9)\theta + (4\alpha^2 - 10\alpha)\theta^2 - 3\alpha^2\theta^3\right)}{18},\\
b_2(\theta) &= \frac{2\alpha^2\theta^2\left(6 + (4\alpha - 4)\theta - 3\alpha\theta^2\right)}{9(2\alpha+3)},\\
b_3(\theta) &= \frac{\theta^2\left(3\alpha^2\theta^2 + 10\alpha\theta + 9\right)}{6(\alpha+1)(2\alpha+3)}.
\end{aligned} \tag{14}
$$

3. Time-Accurate LTS-DG Framework

The LTS-DG formulation used here follows the predictor–corrector structure of time-accurate local time stepping. Each element selects its own local time step, constructs a continuous-in-time predictor from the volume residual, and then integrates the surface-operator contributions on each face separately by using the predictor states from neighboring elements. In this work, the local predictor is an MSCERK(q, m) predictor chosen from the family described in Section 2, where q denotes the number of stored time levels and m denotes the number of current-step stages. Its stage residuals are generated from the element-local volume operator only, so the prediction step remains cell-local; all inter-element coupling is deferred to the face-wise correction.

Let Ω^e denote one DG element and let $\hat{U}^e(t)$ be the vector of its local degrees of freedom. After spatial DG discretization, $\mathcal{L}^e$ and C^e denote the elemental volume-residual operator and face-residual operator, respectively. The symbols $\hat{U}^{e,-}$ and $\hat{U}^{e,+}$ are the interior and exterior traces on the element boundary. The semi-discrete system is then written compactly as

$$
\frac{d\hat{U}^e}{dt} = \mathcal{L}^e(\hat{U}^e) + C^e(\hat{U}^{e,-}, \hat{U}^{e,+}). \tag{15}
$$

The operator $\mathcal{L}^e$ is evaluated from element-local data, whereas C^e couples the element to its neighbors through the numerical fluxes. If the element boundary is decomposed into faces $f \subset \partial\Omega^e$, then

$$
C^e(\hat{U}^{e,-}, \hat{U}^{e,+}) = \sum_{f\subset\partial\Omega^e} C_f^e(\hat{U}^{e,-}, \hat{U}^{e,+}), \tag{16}
$$

where C_f^e denotes the contribution of face f.

Each element is assigned an independent local time step Δt^e according to its local stability restriction. Its current local time interval and normalized local time are

$$
I_n^e = [t_n^e, t_{n+1}^e], \qquad t_{n+1}^e = t_n^e + \Delta t^e, \qquad \theta = \frac{t - t_n^e}{\Delta t^e}, \quad 0 \le \theta \le 1.
$$

The index n is local to element Ω^e and does not imply that neighboring elements are at the same time level. A continuous state $\widetilde{U}^e(t)$ on I_n^e can be obtained either by a conventional continuous explicit Runge–Kutta (CERK) predictor or by a Cauchy–Kowalevski expansion. The present work follows the CERK-type route and uses the MSCERK predictor of Section 2; in this DG setting, the vector field $F(\cdot)$ in the MSCERK formulas is instantiated by the internal volume-residual operator $\mathcal{L}^e(\cdot)$.

Both the volume and surface terms are integrated in time. For the volume contribution, Gaussian

quadrature is applied directly over the local interval I_n^e:

$$\int_{t_n^e}^{t_{n+1}^e} \mathcal{L}^e(\widetilde{U}^e(t))\,dt \approx \sum_{m=1}^{N_{\text{vol}}^e} \omega_m^e\, \mathcal{L}^e\big(\widetilde{U}^e(t_m^e)\big), \tag{17}$$

where t_m^e and ω_m^e are the temporal quadrature points and weights for the volume contribution of element Ω^e. These volume quadrature points are element-local and are generally different from the face quadrature points introduced below.

At a quadrature time t on face f, the two traces are reconstructed from the continuous predictors of the adjacent elements,

$$\hat{U}^{e,-}(t) = \widetilde{U}^e(t), \qquad \hat{U}^{e,+}(t) = \widetilde{U}^{e_f}(t),$$

where Ω^{e_f} is the neighboring element across face f. Because this neighbor may advance with a different local time step, the time interval associated with face f is partitioned into subintervals,

$$[t_n^e, t_{n+1}^e] = \bigcup_{k=1}^{N_{\text{sub}}^f} [t_{k,\text{L}}^f, t_{k,\text{R}}^f].$$

The face contribution is then evaluated piecewise:

$$\int_{t_n^e}^{t_{n+1}^e} C_f^e(\hat{U}^{e,-}(t), \hat{U}^{e,+}(t))\,dt \approx \sum_{k=1}^{N_{\text{sub}}^f} \sum_{g=1}^{N_t^{f,k}} w_g^{f,k}\, C_f^e(\hat{U}^{e,-}(t_g^{f,k}), \hat{U}^{e,+}(t_g^{f,k})). \tag{18}$$

Here $t_g^{f,k}$ and $w_g^{f,k}$ are the Gaussian quadrature point and weight on the k^{th} subinterval of face f. Since the temporal matching relations are different from face to face, these face quadrature points are generally not identical on different faces and are also not the same as the volume quadrature points t_m^e. At each face quadrature time, the local normalized time is computed separately for the two neighboring elements and inserted into their MSCERK predictors to provide the two traces required by the numerical flux.

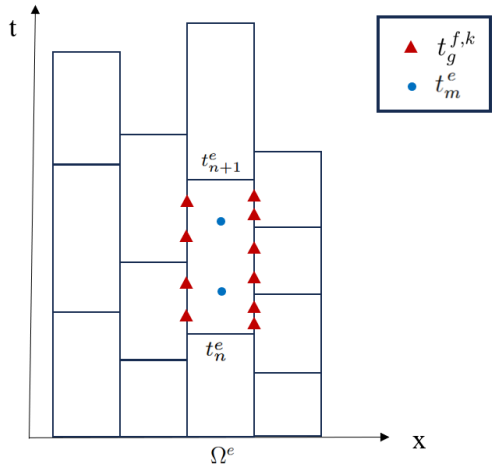

Figure 1: Schematic illustration of temporal quadrature points for the volume and face contributions in a one-dimensional local time-stepping procedure. The blue circles denote the volume quadrature points t_m^e of element Ω^e, while the red triangles denote the face quadrature points $t_g^{f,k}$ used on the piecewise subintervals induced by time-step mismatch across neighboring elements.

The total surface contribution is obtained by summing all face contributions,

$$\int_{t_n^e}^{t_{n+1}^e} C^e(\hat{U}^{e,-}(t), \hat{U}^{e,+}(t))\, dt \approx \sum_{f\subset\partial\Omega^e} \sum_{k=1}^{N_{\text{sub}}^f} \sum_{g=1}^{N_t^{f,k}} w_g^{f,k}\, C_f^e(\hat{U}^{e,-}(t_g^{f,k}), \hat{U}^{e,+}(t_g^{f,k})).$$

When Ω^e reaches t_{n+1}^e, the updated degrees of freedom are obtained from the integrated volume and face-wise surface contributions:

$$\hat{U}^{e,n+1} = \hat{U}^{e,n} + \int_{t_n^e}^{t_{n+1}^e} \mathcal{L}^e(\widetilde{U}^e(t))\, dt + \sum_{f\subset\partial\Omega^e} \int_{t_n^e}^{t_{n+1}^e} C_f^e(\hat{U}^{e,-}(t), \hat{U}^{e,+}(t))\, dt.$$

Equivalently, in quadrature form,

$$\hat{U}^{e,n+1} \approx \hat{U}^{e,n} + \sum_{m=1}^{N_{\text{vol}}^e} \omega_m^e\, \mathcal{L}^e\big(\widetilde{U}^e(t_m^e)\big) + \sum_{f\subset\partial\Omega^e} \sum_{k=1}^{N_{\text{sub}}^f} \sum_{g=1}^{N_t^{f,k}} w_g^{f,k}\, C_f^e(\hat{U}^{e,-}(t_g^{f,k}), \hat{U}^{e,+}(t_g^{f,k})). \tag{19}$$

4. Numerical tests

This section systematically validates the MSCERK time-continuous predictor within the time-accurate LTS-DG framework through three representative test cases: For all local time-stepping calculations, the element-local time step is chosen as

$$\Delta t_e = \frac{\text{CFL}}{2K+1}\, \frac{h_e}{\lambda_e^{\max}}, \tag{20}$$

where K is the polynomial degree, h_e is the characteristic length scale of element Ω^e, and $\lambda_e^{\max}$ is the maximum characteristic wave speed over the element.

(1) Accuracy verification. We consider the one-dimensional Burgers' equation with periodic boundary conditions and the smooth initial condition

$$u(x, 0) = 0.5 \sin(x + 1.0) + 1.0.$$

The computation is performed on a one-dimensional uniform mesh. The final time is $t = 1.0$, and the CFL number is 0.8. Since the solution u varies in space, the local characteristic speed also varies, so the calculation naturally activates different local time steps through Eq. 20. This test is used to assess the spatial and temporal convergence orders and to examine whether the designed order is preserved under variable time stepping. As shown in Table 2, the scheme exhibits approximately fourth-order convergence in both the L^2 and L^∞ norms, consistent with the expected accuracy of the P^3 discretization.

Table 2: Errors and observed convergence orders for the P^3-MSCERK(2,2)-LTS-DG scheme.

N	L^2 error	order	L^∞ error	order
50	5.3802e-06	–	1.5074e-05	–
100	3.6084e-07	3.898	1.1868e-06	3.667
150	7.3659e-08	3.919	2.4394e-07	3.902
200	2.3975e-08	3.902	7.7495e-08	3.986
250	9.5381e-09	4.131	3.2052e-08	3.956

(2) Two-dimensional advected density perturbation. We further consider the inviscid Euler equations with an advected density perturbation on the periodic domain $[0, 2\pi] \times [-\pi/2, \pi/2]$. The exact density

takes the form

$$\rho(x, y, t) = \rho_0 + \varepsilon \sin(k_x(x - ut)) \cos(k_y(y - vt)),$$

with $\rho_0 = 1.0$, $\varepsilon = 0.01$, $k_x = 1$, $k_y = 2$, $(u, v) = (0.45, -0.3)$, constant pressure $p = 1.0$, ratio of specific heats $\gamma = 1.4$, and final time $t = 1$. The test is computed with the P^3-MSCERK(2,2)-LTS-DG scheme. The coarsest 8×4 mesh is shown in Fig. 2; it is a nonuniform, nonaffine quadrilateral mesh, and the finer meshes are generated by connecting physical midpoints. Because the element scales and mappings vary from cell to cell, the local stability restrictions in Eq. 20 produce different local time steps. The CFL number is 0.8.

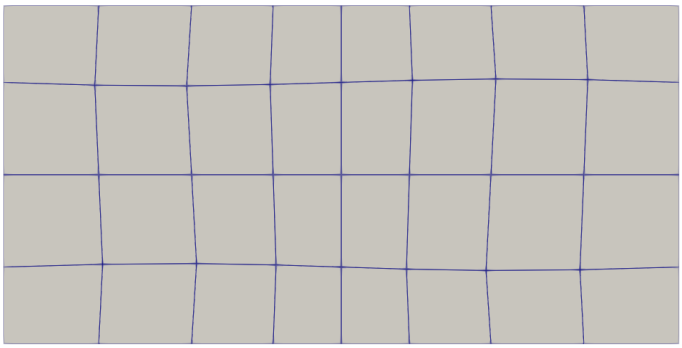

Figure 2: Coarsest 8×4 nonuniform nonaffine quadrilateral mesh for the two-dimensional Euler advected-density perturbation test. Finer levels are generated by midpoint subdivision.

Table 3 reports the convergence behavior. The coarse 8×4 to 16×8 interval remains mildly pre-asymptotic, while the refined levels recover the expected fourth-order accuracy of the P^3 discretization. In particular, the final 32×16 to 64×32 refinement gives orders 4.0196 in the L^2 norm and 3.8235 in the L^∞ norm.

Table 3: Accuracy of the P^3-MSCERK(2,2)-LTS-DG scheme for the two-dimensional Euler advected-density perturbation test.

n_x	n_y	cells	L^2 error	order	L^∞ error	order
8	4	32	1.547357e-04	–	1.832420e-04	–
16	8	128	1.124562e-05	3.7824	2.164394e-05	3.0817
32	16	512	6.276053e-07	4.1634	1.006865e-06	4.4260
64	32	2048	3.869516e-08	4.0196	7.111808e-08	3.8235

(3) $30p30n$ **benchmark case.** A $30p30n$ benchmark case, following Zhang et al, [15], is employed to assess the sensitivity of the LTS time-continuous predictor to time-step variations. This classic high-lift airfoil was developed by McDonnell Douglas in the early 1990s and has been widely studied in academic research, especially with regard to slat noise [15, 16, 17, 18]. Based on the stowed chord length ($c_s = 0.4572$ m), the Reynolds number is 1.71×10^6 at Ma = 0.17. The freestream incidence angle is set to 5.5°, and the CFL number is 0.8.

The three-dimensional mesh contains 499,120 elements and 31.9 million degrees of freedom under polynomial order $p = 3$, with boundary-layer and geometric mesh growth rate of 1.2. The mesh, shown in Fig. 3, is the same one used in the FR simulations of [15]. The computational domain extends $50c_s$ in the upstream and vertical directions and $60c_s$ downstream, while the spanwise width is $c_s/9$ following the BANC-III setup [19]. Local refinement is concentrated near the slat, main element, flap, and wall boundary layers, naturally introducing strong local time-step variations. As shown in Fig. 4, the maximum and minimum time-steps differ by two orders of magnitude.

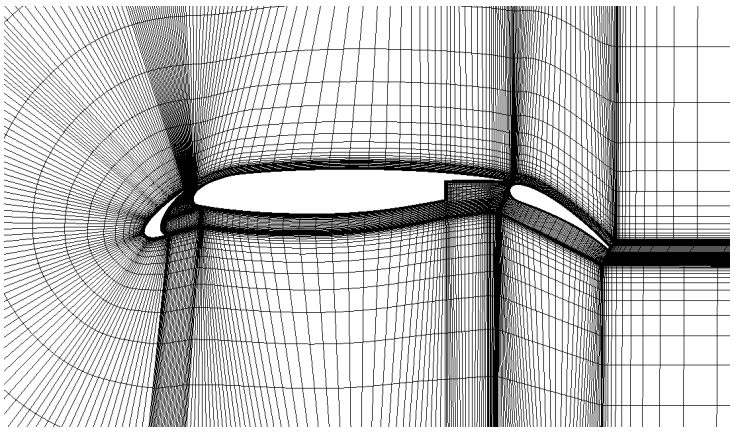

Figure 3: Computational mesh of the 30p30n high-lift airfoil.

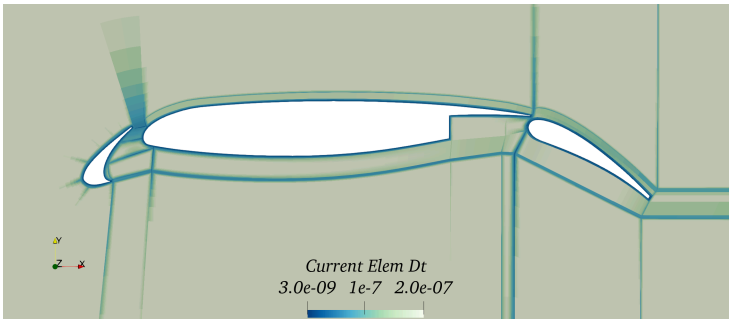

Figure 4: Time-step distribution for the 30p30n case.

Figure 5 compares the instantaneous flow structures using Q-criterion iso-surfaces. The corresponding wall-pressure PSDs at four representative locations (bandwidth $\Delta f = 100$ Hz) are shown in Fig. 6, with comparisons against experimental data [20, 21, 22, 23] and numerical predictions [24, 25, 26]. The MSCERK(2,2) results remain in close agreement with the CERK reference over the frequency range of interest.

Overall, MSCERK(2,2) reduces the computational cost by 27.1% while yielding negligible changes in C_L and C_D, as detailed in Table 4.

Table 4: Efficiency and aerodynamic coefficients in the 30p30n benchmark case.

Scheme	Time cost for 1×10^{-5} s (s)	Cost reduction	$C_L(\Delta C_L)$	$C_D(\Delta C_D)$
CERK	37.97	–	2.973(–)	0.428(–)
MSCERK(2,2)	27.67	27.1%	2.971(-0.09%)	0.425(-0.70%)

5. Conclusions

This work targets the need for time-continuous temporal predictors in time-accurate local time stepping for high-order DG methods. We propose a family of multistep, multistage continuous explicit Runge–Kutta predictors and embed them into a LTS-DG predictor–corrector framework to enable time-accurate interface-flux matching and conservative updates under time asynchrony. In contrast to conventional single-step continuous-extension explicit RK predictors, the key idea of MSCERK is to incorporate information from previous steps into the continuous-extension structure of the current step, thereby distributing the information required for a time-continuous representation across multiple time steps. As a result, for a prescribed target temporal order and while retaining the advantages of a time-continuous

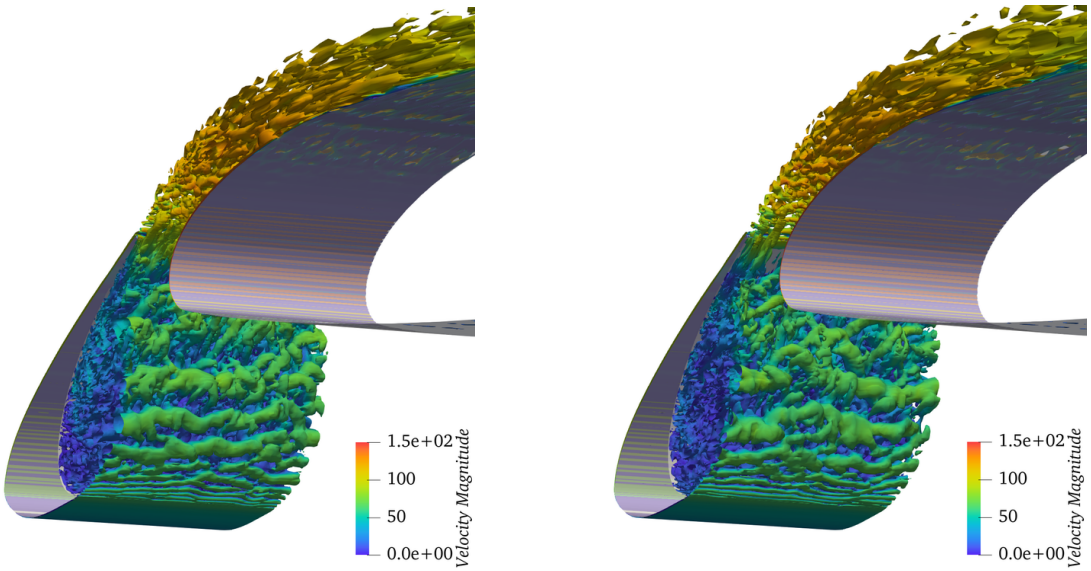

(a) CERK (b) MSCERK(2,2)

Figure 5: Instantaneous Q-criterion iso-surface ($Q = 2 \times 10^6$), colored by velocity magnitude.

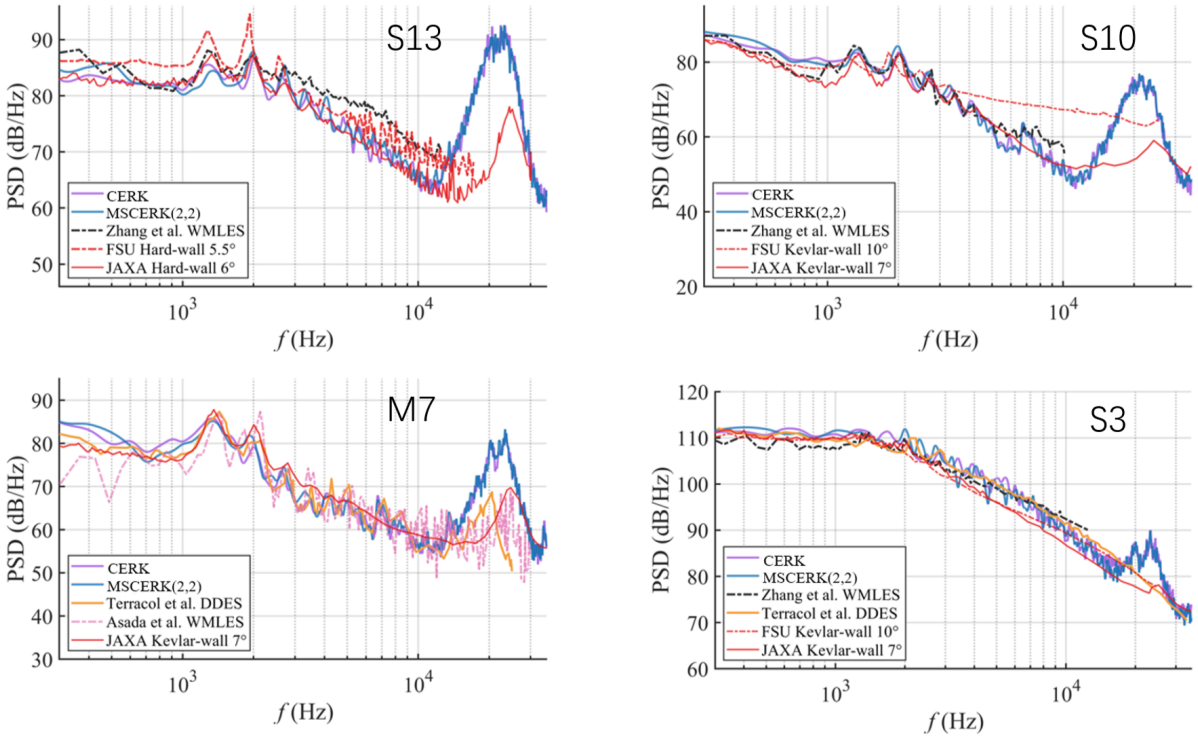

Figure 6: Wall-pressure PSD comparisons at four representative locations, with experimental data from [20, 21, 22, 23] and numerical predictions from [24, 25, 26].

predictor, MSCERK reduces the minimum number of stages needed in each step to achieve the same continuous order. This directly lowers the number of predictor-stage RHS evaluations and related local computations in LTS settings, while preserving the structural benefits of time-continuous representations for time integration/interpolation of asynchronous interface fluxes and subcycling/hierarchical time grids.

The two-step order conditions summarized in this paper provide a compact algebraic basis for constructing MSCERK predictors of different continuous orders. Numerical results show that the MSCERK(2,2)-based LTS-DG scheme preserves the designed accuracy in the one-dimensional smooth test and in the two-dimensional Euler advected-density perturbation test on nonuniform nonaffine meshes, and reduces the computational cost in the 30p30n benchmark while producing results close to the CERK reference. Future work will focus on extending the MSCERK family to higher orders and broader step-ratio variations, and on systematically analyzing stability and error propagation under deeper LTS hierarchies.

Acknowledgements

Although the first author is currently affiliated with the Institute of Engineering Thermophysics, Chinese Academy of Sciences, the main part of this work was completed during his previous appointment at the Department of Mathematics, KTH Royal Institute of Technology, and KTH is therefore listed as his affiliation in this paper. The authors also gratefully acknowledge Rankyee Technology (Beijing) Co., Ltd. for providing the computational resources used for the final $30p30n$ benchmark simulation.

References

[1] Sigal Gottlieb and David I. Ketcheson. Chapter 21 - time discretization techniques. In *Handbook of Numerical Methods for Hyperbolic Problems*, volume 17 of *Handbook of Numerical Analysis*, pages 549–583. Elsevier, 2016.

[2] David I. Ketcheson, Sigal Gottlieb, and Colin B. Macdonald. Strong stability preserving two-step Runge–Kutta methods. *SIAM Journal on Numerical Analysis*, 49(6):2618–2639, 2011.

[3] Xueyu Qin, Xin Zhang, Jian Yu, and Chao Yan. A novel Lax–Wendroff type procedure of two-derivative time-stepping schemes for Euler and Navier–Stokes equations. *Communications in Nonlinear Science and Numerical Simulation*, 140:108436, 2025.

[4] Bernardo Cockburn and Chi-Wang Shu. Runge–Kutta discontinuous Galerkin methods for convection-dominated problems. *Journal of Scientific Computing*, 16(3):173–261, 2001.

[5] Jan S. Hesthaven and Tim Warburton. *Nodal Discontinuous Galerkin Methods: Algorithms, Analysis, and Applications*, volume 54 of *Texts in Applied Mathematics*. Springer, 2008.

[6] Hung T. Huynh. A flux reconstruction approach to high-order schemes including discontinuous Galerkin methods. In *18th AIAA Computational Fluid Dynamics Conference*, 2007. AIAA Paper 2007-4079.

[7] Francesco Bassi and Stefano Rebay. A high-order accurate discontinuous finite element method for the numerical solution of the compressible Navier–Stokes equations. *Journal of Computational Physics*, 131(2):267–279, 1997.

[8] Douglas N. Arnold, Franco Brezzi, Bernardo Cockburn, and L. Donatella Marini. Unified analysis of discontinuous Galerkin methods for elliptic problems. *SIAM Journal on Numerical Analysis*, 39(5):1749–1779, 2002.

[9] Eleuterio F. Toro. *Riemann Solvers and Numerical Methods for Fluid Dynamics: A Practical Introduction*. Springer, Berlin, 3 edition, 2009.

[10] Gregor J. Gassner, Florian Hindenlang, and Claus-Dieter Munz. A Runge–Kutta based discontinuous Galerkin method with time accurate local time stepping. In *Adaptive High-Order Methods in Computational Fluid Dynamics*. World Scientific, 2011.

[11] Gregor J. Gassner, Michael Dumbser, Florian Hindenlang, and Claus-Dieter Munz. Explicit one-step time discretizations for discontinuous Galerkin and finite volume schemes based on local predictors.

Journal of Computational Physics, 230(11):4232–4247, 2011.

[12] Olindo Zanotti, Francesco Fambri, Michael Dumbser, and Arturo Hidalgo. Space–time adaptive ADER discontinuous Galerkin finite element schemes with a posteriori sub-cell finite volume limiting. *Computers & Fluids*, 118:204–224, 2015.

[13] Michael Dumbser, Christophe Enaux, and Eleuterio F. Toro. A unified framework for the construction of one-step finite volume and discontinuous Galerkin schemes on unstructured meshes. *Journal of Computational Physics*, 227(18):8209–8253, 2008.

[14] Brynjulf Owren and Marino Zennaro. Derivation of efficient, continuous, explicit Runge–Kutta methods. *SIAM Journal on Scientific and Statistical Computing*, 13(6):1488–1501, 1992.

[15] Keli Zhang, Peiqing Liu, Shizhi Lin, Kai Liu, and Yi Lu. Sweep effects on slat tonal noise. *AIAA Journal*, 64(6):3399–3420, 2026.

[16] Keli Zhang, Shizhi Lin, Peiqing Liu, Zhibo Zhang, Shihao Liu, Can Fang, Kai Liu, Yi Lu, and Yu Lv. Cfd-based aerodynamic and aeroacoustic optimization of the 30p30n high-lift airfoil. In *32nd AIAA/CEAS Aeroacoustics Conference (2026)*, page 3256, 2026.

[17] Keli Zhang, Shizhi Lin, Peiqing Liu, Shihao Liu, Yuping Ren, Kai Liu, Yi Lu, and Yu Lv. Aeroacoustic control of slat noise: Dependence of noise reduction on angle-of-attack using a novel staggered serration design. In *32nd AIAA/CEAS Aeroacoustics Conference (2026)*, page 3208, 2026.

[18] Keli Zhang, Zhibo Zhang, Shizhi Lin, Peiqing Liu, and Shihao Liu. Multiple deep learning surrogate models for aeroacoustic prediction of the 30p30n high-lift airfoil. In *32nd AIAA/CEAS Aeroacoustics Conference (2026)*, page 3450, 2026.

[19] Meelan M Choudhari and David P Lockard. Assessment of slat noise predictions for 30p30n high-lift configuration from banc-iii workshop. In *21st AIAA/CEAS aeroacoustics conference*, page 2844, 2015.

[20] Mitsuhiro Murayama, Kazuyuki Nakakita, Kazuomi Yamamoto, Hiroki Ura, Yasushi Ito, and Meelan M Choudhari. Experimental study on slat noise from 30p30n three-element high-lift airfoil at jaxa hard-wall lowspeed wind tunnel. In *20th AIAA/CEAS aeroacoustics conference*, page 2080, 2014.

[21] Mitsuhiro Murayama, Yuzuru Yokokawa, Hiroki Ura, Kazuyuki Nakakita, Kazuomi Yamamoto, Yasushi Ito, Takehisa Takaishi, Ryotaro Sakai, Keiji Shimoda, Takayuki Kato, et al. Experimental study of slat noise from 30p30n three-element high-lift airfoil in jaxa kevlar-wall low-speed wind tunnel. In *2018 AIAA/CEAS Aeroacoustics Conference*, page 3460, 2018.

[22] Kyle Pascioni, Louis N Cattafesta, and Meelan M Choudhari. An experimental investigation of the 30p30n multi-element high-lift airfoil. In *20th AIAA/CEAS aeroacoustics conference*, page 3062, 2014.

[23] Kyle A Pascioni and Louis N Cattafesta. Aeroacoustic measurements of leading-edge slat noise. In *22nd AIAA/CEAS aeroacoustics conference*, page 2960, 2016.

[24] Yufei Zhang, Haixin Chen, Kan Wang, and Meng Wang. Aeroacoustic prediction of a multi-element airfoil using wall-modeled large-eddy simulation. *AIAA Journal*, 55(12):4219–4233, 2017.

[25] Marc Terracol, Eric Manoha, Mitsuhiro Murayama, and Kazuomi Yamamoto. Aeroacoustic calculations of the 30p30n high-lift airfoil using hybrid rans/les methods: modeling and grid resolution effects. In *21st AIAA/CEAS Aeroacoustics Conference*, page 3132, 2015.

[26] Hiroyuki Asada, Seiya Sato, Naoki Miwa, and Soshi Kawai. Aeroacoustics simulations using kinetic-energy and entropy preserving (keep) schemes. In *30th AIAA/CEAS Aeroacoustics Conference (2024)*, page 3244, 2024.